Applied Physics A (2023) 129:210
https://doi.org/10.1007/s00339-023-06508-1

Applied Physics A
Materials Science & Processing

Resistive switching behavior in ZnO:Ca thin films deposited by a pulsed laser deposition technique

I. H. Mejri[1] · K. Omri[1] · I. Ghiloufi[1,2] · J. P. B. Silva[3,4] · M. J. M. Gomes[3,4] · L. El Mir[1,2]

Received: 8 November 2022 / Accepted: 15 February 2023 / Published online: 24 February 2023
© The Author(s) 2023

Abstract

Calcium-doped ZnO (CZO) nanopowders were synthesized using the sol–gel method. The structural characteristics were investigated by X-ray diffraction (XRD) and the analysis reveals that our samples are crystalized in a wurtzite hexagonal structure. The morphological properties and the chemical composition of the nanoparticles were studied by transmission electron microscopy (TEM), scanning electron microscopy (SEM), and energy-dispersive X-ray spectroscopy (EDX). The obtained powders are stoichiometric with crystallites in a nanometric scale aggregated in micrometric particles. Then, pulsed laser deposition (PLD) technique was used to grow Ca-doped ZnO thin films with different doping concentrations (1, 3, and 5%), on p-type Si substrates. The Ca doping effect on the electrical properties of the CZO films was investigated by current–voltage characteristics. A resistive switching (RS) effect was observed in the ITO/ZnO:Ca/Au structures. The RS behavior is dependent on the Ca doping concentration. The charge transport mechanisms of the devices were studied. In the positive bias voltage region, the transport is dominated by Ohmic and space-charge limited conduction mechanisms under low and high electric fields, respectively.

Keywords Ca-doped ZnO nanoparticles · ZnO:Ca thin films · Pulsed laser deposition · Resistive switching · Sol–gel

1 Introduction

Recently, non-volatile Random Access Memories (RAMs) have been developed for data storage applications. The RAMs can be divided into magnetic RAMs, ferroelectric RAMs, and resistive (RRAMs) [1–3]. Among them, RRAMs exhibit a simple structure, lower power consumption, high storage density, and higher response speed [4–6]. The phenomenon behind RRAMs is resistive switching, where under an appropriate external electric field, the device can be reversibly switched between a high resistance state (HRS) and a low resistance state (LRS). These transitions from HRS to LRS and conversely from LRS to HRS are defined as the SET and RESET switching, respectively. In addition, many studies proved the existence of two resistive switching modes: unipolar and bipolar switching which are related to the various material systems and the different switching mechanisms [7]. Therefore, resistive switching can be a uniform phenomenon that scales proportionally with the total area of the switching material. On the other hand, it can be

✉ J. P. B. Silva
josesilva@fisica.uminho.pt

I. H. Mejri
ines.mejrihajjej24@gmail.com

K. Omri
omrikarim16@gmail.com

I. Ghiloufi
ghiloufimed@yahoo.fr

M. J. M. Gomes
mjesus@fisica.uminho.pt

L. El Mir
Lassaad.ElMir@fsg.rnu.tn

[1] Laboratory of Physics of Materials and Nanomaterials Applied at Environment (LaPhyMNE), Faculty of Sciences in Gabes, Gabes University, 6072 Gabes, Tunisia

[2] Department of Physics, College of Sciences, Al Imam Mohammad Ibn Saud Islamic University (IMSIU), Riyadh 11623, Saudi Arabia

[3] Physics Center of Minho and Porto Universities (CF-UM-UP), University of Minho, Campus de Gualtar, 4710-057 Braga, Portugal

[4] Laboratory of Physics for Materials and Emergent Technologies, LapMET, University of Minho, 4710-057 Braga, Portugal

a question of a localized phenomenon that is based on the rupture and the formation of the conducting filaments (CF). Indeed, the formation of the CF in the resistive switching layer causes the change of the device to LRS, however, when the CF is ruptured, the device switched back to the HRS. Since the resistive switching effect is based on charge defect migration [8], these two behaviors of CF formation and rupture can be presented as the migration of the anion or cation under an applied voltage accompanied by an electrochemical reaction of the metal or oxygen vacancies. Various materials including ZrO_2 [9], TiO_2 [10], ZnO [11], and HfO_2 [12] have been investigated for RRAMs. Among these materials, zinc oxide (ZnO) semiconductor has been widely studied because of their important structural, optical, and electrical properties [13–15]. Moreover, doping is often used to control the defect concentration in order to improve their properties [16–18]. From the literature, the resistive switching phenomena reported are based on doped ZnO. X. Zhao et al. [19] have reported the RS characteristics of Li-doped ZnO (LZO) thin films based on magnetron sputtering. They have found that with the addition of LZO, the ON/OFF current ratio and the set voltage of the devices Pt/Ag/ZnO:Li/Pt/Ti increases. In addition, they have reported that the devices can quickly transform from an HRS to an LRS with a good endurance of more than 10^3 cycles at an applied pulse voltage and long retention of up to 10^4 s. Furthermore, A. Younis et al. [20] have studied the RS behavior of Ti-doped ZnO thin films prepared by a facile electrochemical deposition method. These films exhibit excellent resistance-switching behavior with HRS/LRS ratio of about 14 during the endurance test much better than undoped ZnO. In addition, S. S. Li et al. [21] have investigated the RS phenomenon of Cr-doped ZnO thin films.

Among the doping elements that were suggested for the doping of ZnO nanopowder, we note calcium. Ca-doped ZnO has attracted great interest from researchers in different fields of semiconductor applications [22–24]. Therefore, to magnify the potential of Ca-doped ZnO resistive switching for application in non-volatile memories, the electrical characteristic properties of these devices should be studied. Therefore, in this paper, we investigated the calcium concentration effect on the structure electrical and bipolar resistive switching properties of ITO/ZnO:Ca/Si (p)/Au thin films.

2 Experimental details

Calcium-doped ZnO nanopowders were synthesized by sol–gel method following the protocol of El Mir et al. [25, 26]. Indeed, we dissolved 16 g of zinc acetate dehydrate [Zn $(CH_3COO)_2$. $2H_2O$; 99%] in 112 mL of methanol. After 10 min of magnetic stirring at room temperature, we added an adequate quantity of calcium chloride hexa-dehydrate [$CaCl_2$, $6H_2O$] that correspond to [Ca/Zn] atomic ratios of 0.01, 0.03, and 0.05. For drying the obtained solution, it was placed in an autoclave under supercritical conditions of ethyl alcohol ($P_c = 63.6$ bars, $T_c = 243$ °C). Then, the obtained nanopowders were pressed inside the target holders of 2 inches in diameter with 300 kg/cm^2 uniaxial pressure to obtain compact targets. Then, calcium-doped thin films with 1, 3, and 5% doping concentrations have been deposited on a p-type silicon substrate (111) of a resistivity 1–20 Ω, using a pulsed laser deposition technique (PLD/MBE 2100) from PVD products [27]; the source of excitation is KrF excimer Laser (wavelength $\lambda = 248$ nm, repetition rate of 10 Hz and pulse width 20 ns) working at 350 mJ to ablate the target. The growth pressure and temperature are 10^{-6} Torr and 300 °C, respectively. The target–substrate distance was 5.5 cm. All PLD parameters which may contribute to the deposition rate of the films were kept constant during the operating time, and the film thicknesses measured by Stylus Profiler (Veeco Dektak 150) were about 300 nm. For simplicity, the calcium-doped samples with 1, 3, and 5% doping concentrations were designated as C1ZO, C3ZO, and C5ZO. Finally, to obtain the ITO/ZnO:Ca/Si(p)/Au device, the ITO contacts were deposited by the ion-beam sputtering deposition method as reported previously [28] and the Au contacts were deposited by the thermal evaporation method under vacuum.

The structure of the thin films was characterized by X-ray diffraction (DRX) using CuKα radiation (1.5418 Å) of a Bruker D5005. The surface morphology analysis and the chemical constituent of the nanoparticles were investigated by transmission electron microscopy (TEM), scanning electron microscopy (SEM), and energy-dispersive X-ray spectroscopy (EDX). The oxygen vacancy concentrations (V_O) for the CZO thin films were investigated by x-ray photoelectron spectroscopy (XPS). The spectra were acquired using the K-alpha system of Thermo Scientific, equipped with a monochromatic Al-Kα source (1486.6 eV), operating in a constant analyzer energy (CAE) mode. To fit measured spectral profiles Gauss–Lorentzian-shaped bands were used. The V_O concentrations were estimated from the areas under the photoelectron peaks. The quantification of the surface species was carried out by decomposing the photoelectron spectra. Further, the electrical characteristics were done after deposing the ITO and gold (Au) contacts. The current–voltage (*I–V*) measurements were investigated using a Keithley 617 electrometer.

3 Results and discussion

3.1 Structural and morphological analysis

As shown, Fig. 1 displays the typical XRD pattern of ZnO:Ca nanopowders. The XRD diagrams show nine

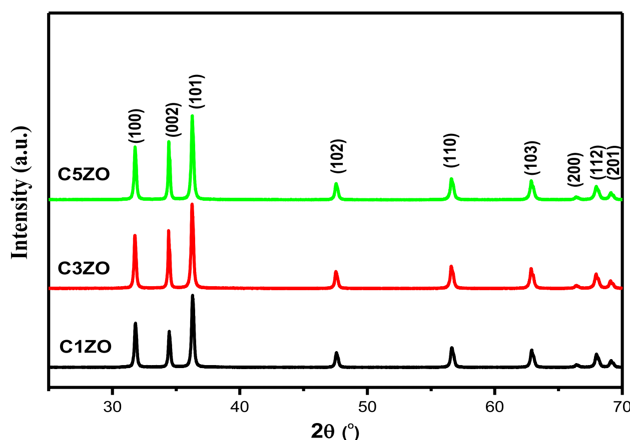

Fig. 1 X-ray diffraction pattern of Ca-doped ZnO nanoparticles

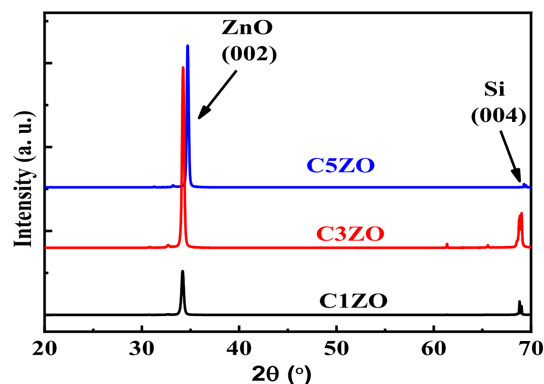

Fig. 2 X-ray diffraction spectra of Ca-doped ZnO thin films

diffraction peaks for all samples with different intensities without the detection of any secondary phases. These diffraction peaks are indexed to the hexagonal Wurtzite structure of ZnO in agreement with the standard JCPDS database (card 36–1451) [29]. Therefore, to determine the crystallite size for our samples, we used Scherrer's formula [30]:

$$D = \frac{0.9\lambda}{\beta \cos\theta} \quad (1)$$

where λ defined the X-ray wavelength (1.5418 Å), θ is the diffraction angle and β represents the full width at half maximum of the XRD peak. Thus, the obtained values increase with the incorporation of Ca content from 41, 42 to 44 nm for C1ZO, C3ZO, and C5ZO, respectively. On the other side, concerning the structural characteristics of CZO thin films with different concentrations of Ca, Fig. 2 depicts the XRD patterns. It is clear the domination of the (002) oriented crystallites of hexagonal Wurtzite structure for all films; this proves the preferred c-axis orientation normal to the surface [31]. Further, the absence of additional peaks in the XRD patterns excludes the possibility of any secondary phase and indicates that these films have a high-quality crystalline structure. Further, a small shift to the higher angle with the increase in the calcium concentration was observed indicating that some residual stress inside the film may exist [32]. Table 1 shows the measured value of the crystallite size from the Debye–Scherrer formula and the lattice parameters for the hexagonal crystalline system calculated from Eqs. (2) and (3) [33]:

$$d^2_{(hkl)} = \left[\frac{4\left(h^2 + k^2 + l^2\right)}{3a^2} + \frac{l^2}{c^2}\right]^{-1} \quad (2)$$

$$2d_{hkl} \sin\theta = n\lambda \quad (3)$$

where 'a' and 'c' are the lattice constants, h, k, and l represent the miller index and d_{hkl} is the interplanar spacing for indices (h, k, l). The lattice constant 'a' is obtained through the relation ($a = \lambda/\sqrt{3}\ \sin\theta$) with the first approximation ($n = 1$) for the (100) plane, and the lattice constant 'c' was derived for the plane (002) ($c = \lambda/\sin\theta$). It is clear that the decrease of the lattice parameter 'a' and 'c' with increasing the Ca concentration indicates the reduction in the oxygen vacancies [34]. Besides, the Ca doping has increased the average crystallite size 'D'. The morphological characteristics, particularly for the C3ZO sample, were investigated by SEM and TEM observations. As deduced by the SEM micrograph presented in Fig. 3, the typical morphology of C3ZO nanoparticles shows round particles having a rough porous fine-grained microstructure. The dimension of these agglomerated particles is between 2 and 5 µm. Then each microparticle is formed by nanostructure which is confirmed by the TEM measurement, presented in Fig. 4. As seen, the Ca-doped sample (C3ZO) is composed of grains with different particle size distributions. These grains show a cylindrical shape with a hexagonal base. The estimated size varies between 20 and 80 nm which is in agreement with that obtained by XRD. Further, the EDX analysis presented in Fig. 5 reports the chemical composition of C3ZO nanopowders. It is clear the presence only of Zn, O, and Ca elements. There are no detectable traces of any contaminant in the C3ZO nanoparticles which confirms that the calcium was totally incorporated in the ZnO. Figure 6 depicts the cross-section SEM image obtained from the C3ZO thin film deposited onto a p-type Si substrate. The image shows a perpendicularly oriented columnar structure. Further, it is clear that the interface between the deposited thin film and the substrate is well-defined and the corresponding film thickness was measured to be around 300 nm with a good quality of the

Table 1 Structural parameters of CZO samples

(002) peak	2 θ (°)	β (°)	D (nm)	d_{hkl} (Å)	c (Å)	A (Å)	V (Å^3)
C1ZO	34.19	0.2398	35	2.623	5.245	3.164	45.47
C3ZO	34.24	0.2225	37	2.619	5.238	3.161	45.32
C5ZO	34.71	0.1961	42	2.584	5.168	3.115	43.42

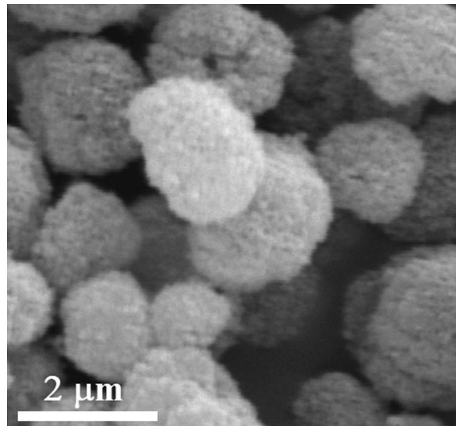

Fig. 3 SEM image of C3ZO nanopowder

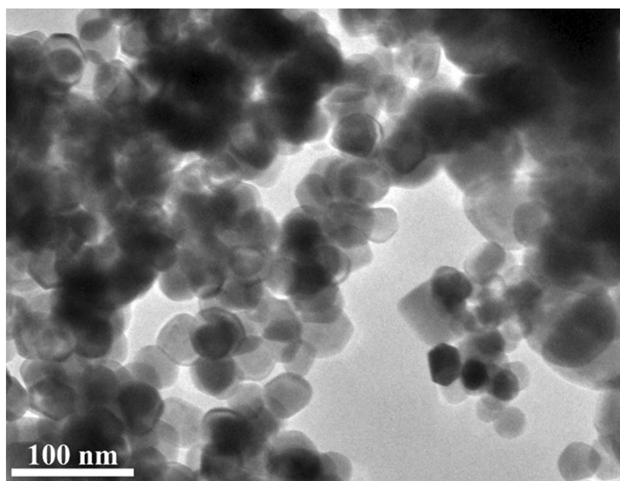

Fig. 4 TEM micrograph of C3ZO nanopowder

surface corresponding to RMS surface roughness of about 12 nm. The XPS spectra of thin films (Fig. 7) confirm the presence of the V_O in the thin films with concentrations of about 3.7, 2.0, and 2.2 for C1ZO, C3ZO, and C5ZO, respectively. This result reinforces the idea that the V_O plays a main role in the transport phenomenon in these samples, and confirms the fact that the increase of Ca loading enhances the crystallinity and reduces the V_O which affects the conductivity of the films and then the resistive switching properties.

3.2 Resistive switching (RS) characteristics

Figure 8(a–c) shows the *I–V* curves of the Ca-doped ZnO with different concentrations of 1, 3, and 5%. It is clear that all samples exhibit a resistive switching behavior. Especially for samples 1, and 3% of Ca, it was observed the bipolar multi-level switching behavior. For C1ZO (a), in the HRS, we can note the presence of 2-step 'Set' behavior with $V_{Set1} = 0.1$ V and $V_{Set2} = 0.6$ V. In addition, for C3ZO (b) there is a 2-step behavior with $V_{Set1} = 0.3$ V, and $V_{Set2} = 0.9$ V, which indicates that the 'Set' behavior of the CZO resistive memory device can be attributed to the effect of the calcium incorporation. We can observe the same behavior for Li-doped ZnO RRAM devices reported by Lin et al. [35]. Furthermore, we can obtain the multi-resistances states by forming various conducting filaments inside the device: ionic and metallic conduction filaments. As reported in the previous studies [36], the metallic conduction filament can be higher than those of the ionic one which may indicate that the metallic filament needs a higher electric field than the ionic filament. Subsequently, M. Liu et al. demonstrate the diffusion of different metals such as Ag or Cu into the oxide in order to obtain the metallic filament. Similarly, in our case, we can confirm that the oxygen vacancies (*ionic filament*), as well as the calcium (*metallic filament*), were responsible for the resistive switching effect. On the other hand, when increasing the applied voltage up to a maximum of 1 V, and then gradually returning to 0 V, all of the devices still maintain in the LRS. The current compliance observed at the voltage sweep region (from 0 V to – 1 V) where we defined the RESET process, we note the transform of the resistance of the device from LRS to HRS. The RS ratio (I_{LRS}/I_{HRS}) is found to be 10^2 for C1ZO and C3ZO at 0.3 V and 0.2 V, respectively.

To examine and clarify the carrier transport mechanism of Ca-doped ZnO thin film devices, we plotted a double logarithmic scale in the positive bias region of the *I–V* curves. As seen, Fig. 9 displays the results of the linear fit of the samples. From these results, it is clear to observe that the ions transport within the RRAM device is dominated by Ohmic behavior under low positive bias. Indeed, For C1ZO, the fitted slope is approximately 0.9 in the HRS, which indicates that the conduction follows the Ohmic conduction mechanism. With increasing the applied voltage, the slope is about 2.2, then 2.6 indicating that the carrier transport mechanism in the HRS and LRS, respectively,

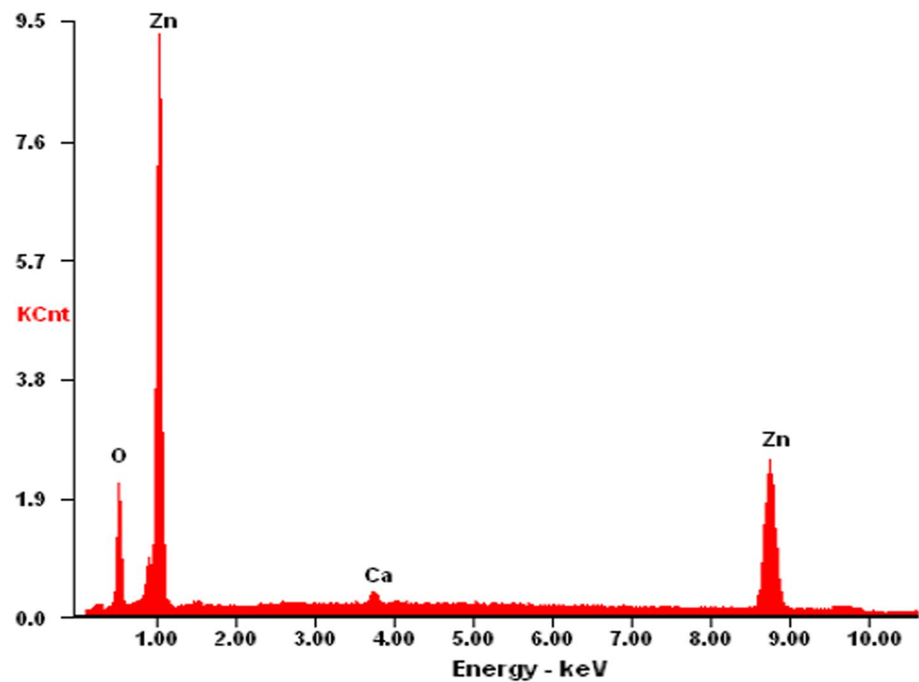

Fig. 5 Chemical composition of C3ZO nanopowder

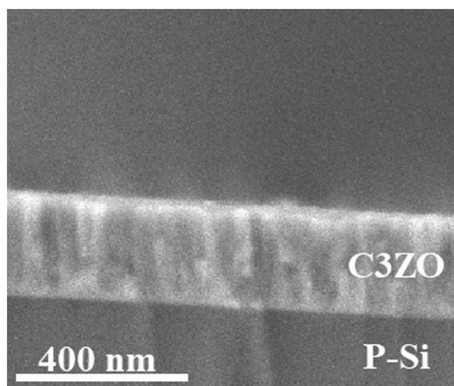

Fig. 6 Cross-section SEM image of the CZO/Si heterojunction (bar scale 400 nm)

follows the trap-controlled space-charge limited conduction (SCLC) model. As the positive voltage decreases, the fitted slope decreases to 0.6 which denotes the Ohmic conduction mechanism. For C3ZO, the fitted slope is approximately 0.6 and increases to 1.6 in the HRS with increasing the applied voltage indicating the Ohmic conduction mechanism. Then, when increasing the voltage, the fitted sloped is about 3.4 in LRS following space-charge limited conduction and decreases to 1.3 which indicates the Ohmic conduction mechanism [37]. On the other hand, the fitted slope in the HRS and LRS for C5ZO is approximately 1.05 which is corresponding to the Ohmic conduction behavior. Therefore, based on the literature [38, 39], we can notice that the generation and the recovery of oxygen vacancies with non-lattice oxygen ions and the SCLC conduction behavior can be employed in order to justify the mechanism of the bipolar resistive switching in the ITO/ZnO:Ca/Au devices. For example, Gao et al. [40] have reported that some defects in the thin films such as oxygen vacancies, grain boundaries, and interstitial atoms present in the thin films, act like a trap center for charge carriers and cause the trap-controlled SCLC. Similar to this study, we can note that the transport of Ca ion and the restoration of the oxygen ions by the calcium ion under the bias voltage may be also a reason for the resistive switching behavior [41].

To further investigate the resistive switching behavior of Ca-doped ZnO thin film devices, we plotted the variation of the resistance at different temperatures in the range of 20–100 °C. As shown in Fig. 10, the resistance of the C3ZO sample was measured under an applied bias voltage of 0.8 and 0.6 V for HRS and LRS, respectively. It can be noticed that the resistance of HRS increases with temperature which indicates the metallic properties [42]. This behavior is similar to the results studied by Li Ying et al. [43]. They have shown that the resistance of the Cu/ZrO_2/ATO device decreases obviously when the temperature decreases which is typical for electronic transport in a Cu metal. Thus, the Cu metallic conduction filament has been formed in the ZrO_2 thin films. However, when the temperature increases, the resistance of LRS decreases which is corresponding to the semiconductor properties [44] and confirms the formation of the ionic filament. So the temperature dependence result proves the formation of ionic and metallic filaments, at various voltages. Further, our result which shows the formation of the metallic filament at a higher voltage than the ionic filament confirms

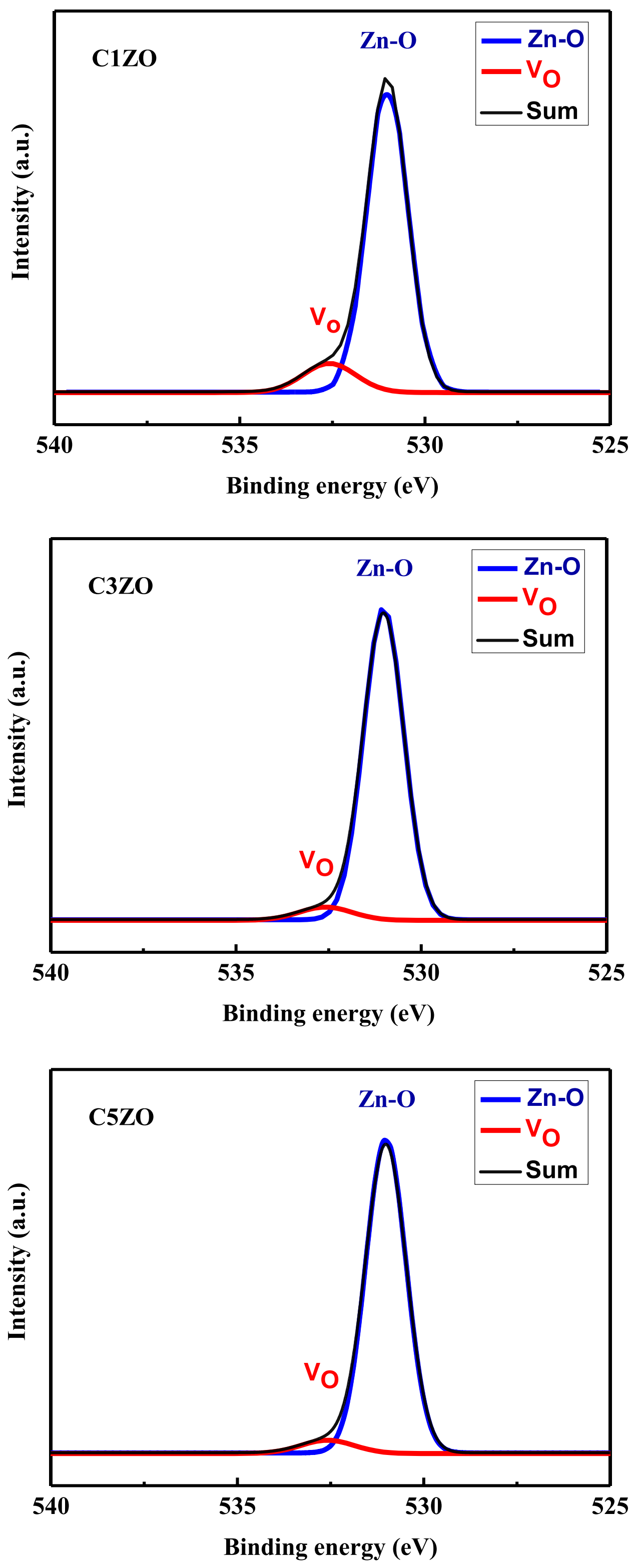

Fig. 7 XPS analyses illustrating the presence of V_O in the thin films

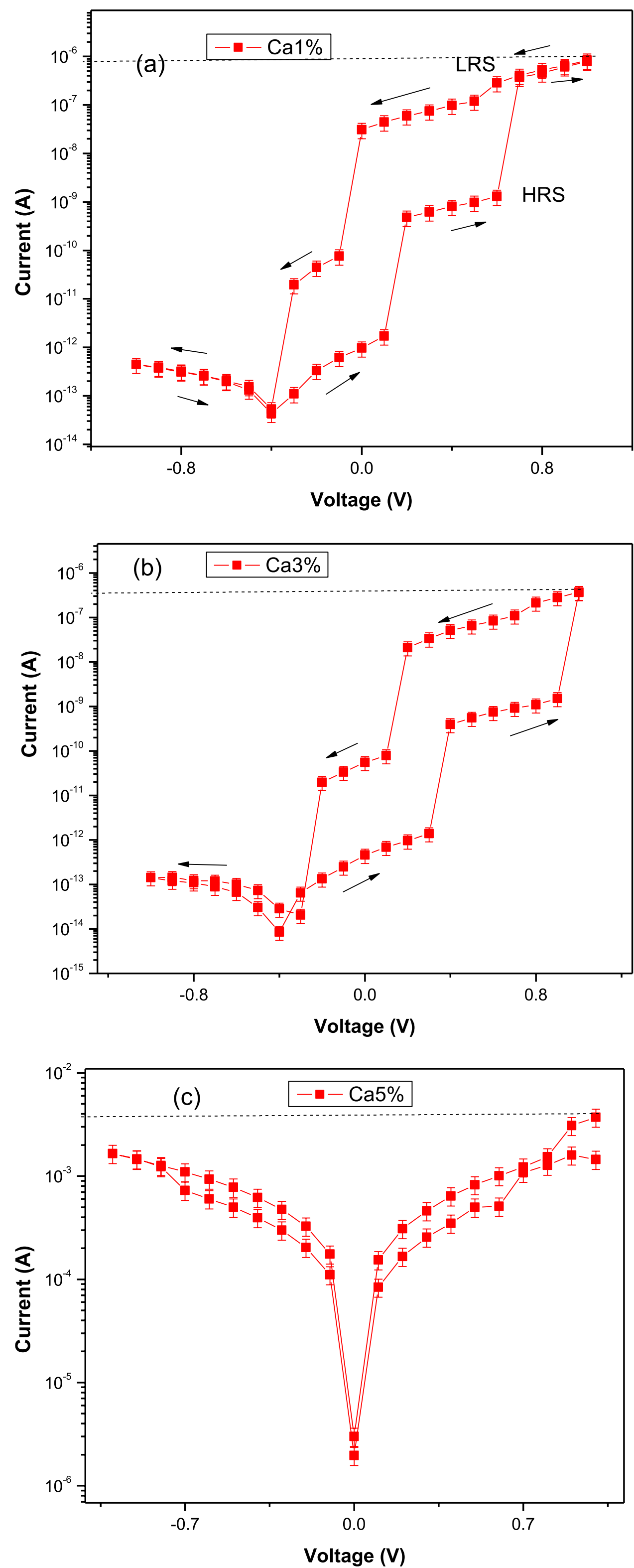

Fig. 8 *I–V* curves of ITO/CZO/Si (p)/Au thin films at different Ca concentrations: **a** C1ZO; **b** C3ZO; **c** C5ZO

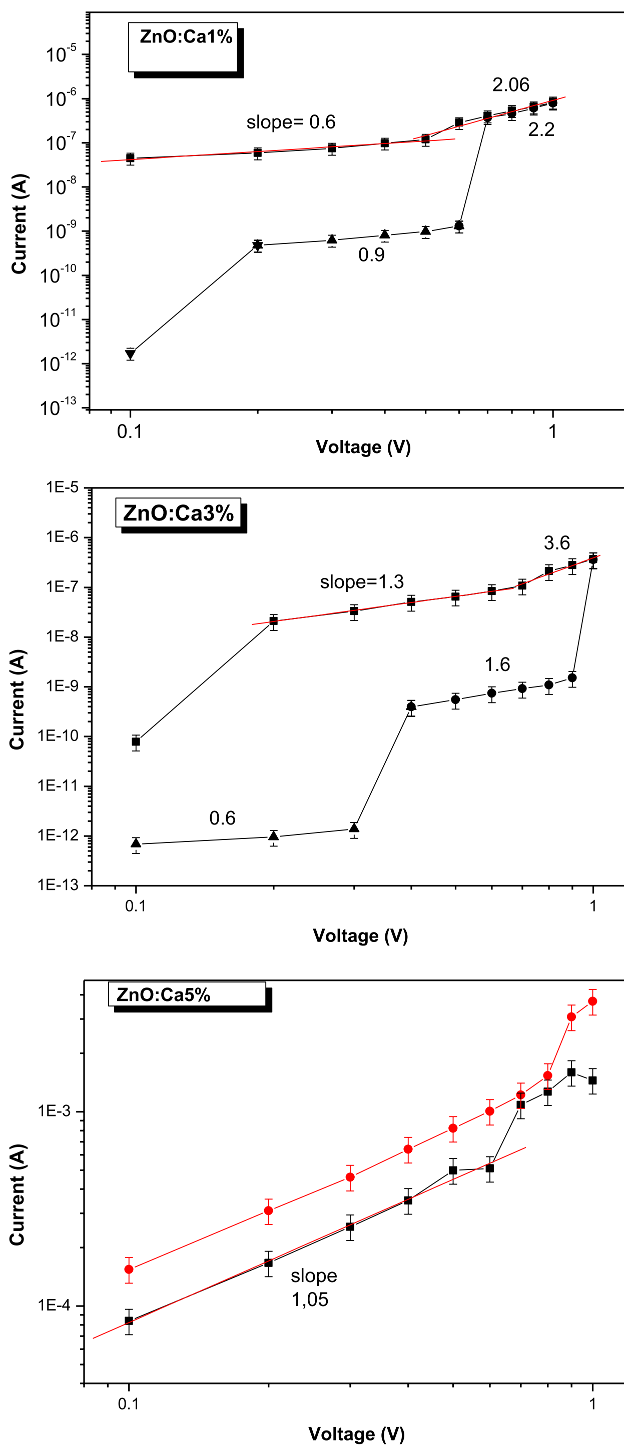

Fig. 9 The linear fitting of the *I*–*V* curves in the positive bias region of C1ZO, C3ZO, and C5ZO samples, in the double logarithmic scale

what we note in the previous paragraph. This behavior is similar to the study reported by F.L. Faita et al. [45] for the hafnium aluminum oxide (HfAlO) thin films deposited by the ion-beam sputtering technique on a silicon substrate.

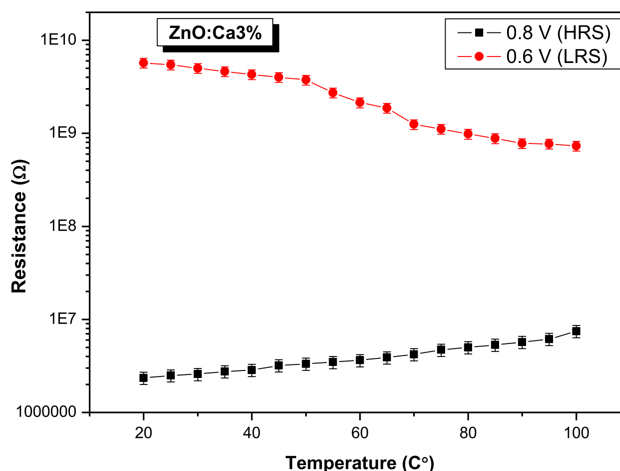

Fig. 10 The variation of the resistance with different temperatures under a bias voltage of 0.8 V for HRS and 0.6 V for LRS

As shown in Fig. 11, we plotted the dark and illuminated *I*–*V* curves. The illuminated ones are shown for two different intensities (L1: 2.38 A and L2: 2.82 A). It is clear to notice that the curves have a shift towards the lower voltage region with the increase of the light intensity. However, the current increases slightly with the light. This result clearly shows the effect of the light intensity on the sample C3ZO, so these processes can be optically activated.

4 Conclusion

Ca-doped zinc oxide thin films were deposited by pulsed laser deposition technique (PLD) onto p-type silicon substrates. From the X-ray diffraction, these films with different Ca contents (1, 3, and 5%) have hexagonal structures

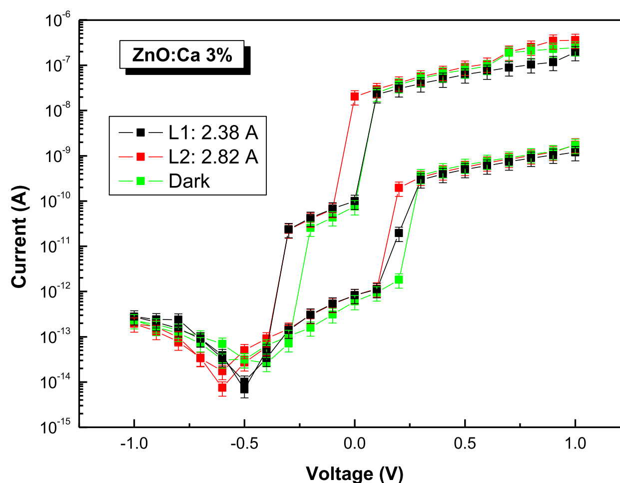

Fig. 11 The dark and illuminated *I*–*V* curves of the C3ZO sample

and the values of the crystallite size were determined using the Debye–Scherrer formula. The TEM image showed a cylindrical shape with a hexagonal base of the grains C3ZO and confirmed the nanometric size. From the SEM, these nanoparticles showed agglomerated particles with dimensions in the range of 2–5 µm, and for C3ZO thin film, the cross-section SEM image showed a perpendicularly oriented columnar structure. The current–voltage measurements revealed the presence of the resistive switching behavior and the oxygen vacancies as well as the calcium were responsible for this phenomenon. Furthermore, two conduction mechanisms were presented in this work; Ohmic and space-charge limited conduction mechanisms. This work demonstrates that Ca doping can further enhance the switching characteristics of ZnO thin films and thus have the potential for next-generation of non-volatile memory applications.

Acknowledgements This work was funded by the National Plan for Sciences, Technology, and innovation (MAARIFAH) – King Abdulaziz City for Sciences and Technology—Kingdom of Saudi Arabia, award number: 13-NAN517-08. This work was supported by the Portuguese Foundation for Science and Technology (FCT) in the framework of the Strategic Funding Contract UIDB/04650/2020.

Funding Open access funding provided by FCT|FCCN (b-on).

Data availability statement Data will be made available on request.

Open Access This article is licensed under a Creative Commons Attribution 4.0 International License, which permits use, sharing, adaptation, distribution and reproduction in any medium or format, as long as you give appropriate credit to the original author(s) and the source, provide a link to the Creative Commons licence, and indicate if changes were made. The images or other third party material in this article are included in the article's Creative Commons licence, unless indicated otherwise in a credit line to the material. If material is not included in the article's Creative Commons licence and your intended use is not permitted by statutory regulation or exceeds the permitted use, you will need to obtain permission directly from the copyright holder. To view a copy of this licence, visit http://creativecommons.org/licenses/by/4.0/.

References

1. S.S. Parkin, K.P. Roche, M.G. Samant, P.M. Rice, R.B. Beyers, J. Appl. Phys. **85**, 5828–5833 (1999)
2. S. Sinharoy, H. Buhay, R. Lampe, M.H. Francombe, J. Vacuum Sci. Technol. A Vacuum Surfaces Films **10**, 1554–1561 (1992)
3. M.C. Kao, H.Z. Chen, K.H. Chen, J.B. Shi, J.H. Weng, K.P. Chen, J. Mater. Chem. C **5**, 10517–10523 (2017)
4. Y. Li, S. Long, M. Zhang, Q. Liu, L. Shao, S. Zhang, Y. Wang, Q. Zuo, S. Liu, M. Liu, IEEE Electron Device Lett. **31**, 117–119 (2009)
5. M. Zackriya, H.M. Kittur, A. Chin, Sci. Rep. **7**, 1–7 (2017)
6. Y.S. Fan, P.T. Liu, C.H. Hsu, Thin Solid Films **549**, 54–58 (2013)
7. F. Pan, C. Chen, Z. Wang, J. Yang, F. Zeng, Mater. Int. **20**, 1–15 (2010)
8. P. Gonon, M. Mougenot, C. Vallee, C. Jorel, V. Jousseaume, H. Grampeix, F. El Kamel, J. Appl. Phys. **107**, 074507 (2010)
9. Y. Li, X. Li, L. Fu, R. Chen, H. Wang, X. Gao, IEEE Trans. Electron Devices **65**, 5390–5394 (2018)
10. Y.M. Lu, M. Noman, Y.N. Picard, J.A. Bain, P.A. Salvador, M. Skowronski, J. Appl. Phys. **113**, 163703 (2013)
11. S. Lee, H. Kim, D.J. Yun, S.W. Rhee, K. Yong, Appl. Phys. Lett. **95**, 262113 (2009)
12. E. Perez, C. Wenger, A. Grossi, C. Zambelli, P. Olivo, J. Vacuum Sci. Technol. B Nanotechnol. Microelectron. Mater. Process. Measurem. Phenomena **35**, 01A103 (2017)
13. R. Dhahri, M. Hjiri, L. El Mir, A. Bonavita, D. Iannazzo, S.G. Leonardi, G. Neri, J. Appl. Surf. Sci. 355 (2015) 1321–1326.
14. M. Mahmoud, K. Echabaane, L.E. Omri, R.B.C. Mir, J. Alloys Compd. **786**, 960–968 (2019)
15. S. Amara, I. Ben Slama, I. Mrad, N. Rihane, W. Khemissi, L. El Mir, K. Ben Rhouma, H. Abdelmelek, M. Sakly, J. Hum. Experim. Toxicol. 31 (2015) 1202–1209.
16. L. El Mir, J. Lumin. **186**, 98–102 (2017)
17. R. Dhahri, M. Hjiri, L. El Mir, A. Bonavita, D. Iannazzo, M. Latino, N. Donato, S.G. Leonardi, G. Neri, J. Phys. D Appl. Phys. **49**, 135502–135508 (2016)
18. S. Amara, I. Ben Slama, I. Mrad, N. Rihane, W. Khemissi, L. El Mir, K. Ben Rhouma, H. Abdelmelek, M. Sakly, Toxicol. Indust. Health 31 (12), (2015) 1202–1209.
19. X. Zhao, Y. Li, C. Ai, D. Wen, Materials **12**, 1282 (2019)
20. D. Younis, Chu, S. Li, Nanoscale Res. Lett. **8**, 1–6 (2013)
21. S.S. Li, Y.K. Su, RSC Adv. **9**, 2941–2947 (2019)
22. M.-S. Cao, X.-X. Wang, M. Zhang, J.-C. Shu, Wen- Qiang Cao, Hui-Jing Yang, Xiao-Yong Fang, Jie Yuan. Adv. Func. Mater. **29**, 1807398 (2019)
23. W. Yu, D. Han, P. Shi, Y. Cong, Y. Zhang, J. Dong, X. Zhou, L. Huang, G. Cui, S. Zhang, X. Zhang, Y. Wang, Electron. Lett. **51**, 1286–1288 (2015)
24. I. Istrate, F. Nastase1,I. Mihalache,F. Comanescu, ,R. Gavrila, O. Tutunaru,C. Romanitan, V. Tucureanu, M. Nedelcu, R. Müller, Journal of Sol-Gel Science and Technology, 92 (2019) 585–597.
25. L. El Mir, K. Omri, Superlattices Microstr. **75**, 89–98 (2014)
26. L. El Mir, A. Amlouk, C. Barthou, S. Alaya, Physica B **388**, 412 (2007)
27. K. Omri, A. Alyamani, L. El Mir, J. Mater. Sci. Mater. Electron. **30**, 16606–16612 (2019)
28. J. P. B. Silva, K. C. Sekhar, F. Cortés Juan, R. F. Negrea, A. C. Kuncser, J. P. Connolly, C. Ghica, J. Agostinho Moreira, Solar Energy, 167 (2018) 18–23.
29. S. Muthukumaran, R. Gopalakrishnan, Opt. Mater. **34**, 1946–1953 (2012)
30. B. D. Cullity, Addison-Wesley, Reading, MA, 102 (1978).
31. K. Ellmer, R. Cebulla, R. Wendt, Thin Solid Films **317**, 413 (1998)
32. J.W. Jeon, M. Kim, L.W. Jang, J.L. Hoffman, N.S. Kim, I.H. Lee, Electron. Mater. Lett. **8**, 27–32 (2012)
33. U. Godavarti, V.D. Mote, M. Dasari, J. Asian Ceramic Societies **5**, 391–396 (2017)
34. O. Biligili, Acta Physica Polonica **136**, 460–466 (2019)
35. C.C. Lin, J.F. Tang, H.H. Su, C.S. Hong, C.Y. Huang, S.Y. Chu, J. Appl. Phys. **119**, 244506 (2016)
36. M. Liu, Z. Abid, W. Wang, X. He, Q. Liu, W. Guan, Appl. Phys. Lett. **94**, 233106 (2009)
37. P.R.S. Reddy, V.R. Nallagatla, Y.A. Kumar, G. Murali, Progress Natl. Sci. Mater. Int. **32**, 602–607 (2022)
38. N. Xu, L. Liu, X. Sun, X. Liu, D. Han, Y. Wang, R. Han, J. Kang, B. Yu, Appl. Phys. Lett. **92**, 232112 (2008)

39. M. Ismail, C.Y. Huang, D. Panda, C.J. Hung, T.L. Tsai, J.H. Jieng, C.A. Lin, U. Chand, A.M. Rana, E. Ahmed, I. Talib, M.Y. Nadeem, T.Y. Tseng, Nanoscale Res. Lett. **9**, 1–8 (2014)
40. S.M. Gao, H. Wang, J.W. Xu, C.L. Yuan, X.W. Zhang, Solid State Electron. **76**, 40–43 (2012)
41. U. Ozgur, Y.I. Alivov, C. Liu, A. Teke, M.A. Reshchikov, S. Dogan, V. Avrutin, S.J. Cho, H. Morkoc, J. Appl. Phys. **98**, 11 (2005)
42. E. Perez, C. Wenger, A. Grossi, C. Zambelli, P. Olivo, R. Roelofs, J. Vaccum Sci. Technol. B Nanotechnol. Microelectron. Mater. Process. Measurem. Phenomena **35**, 01A103 (2017)
43. Y. Li, G. Zhao, J. Su, E. Shen, Y. Ren, Bull. Mater. Sci. **37**, 455–460 (2014)
44. W. Wang, Y. Li, W. Yue, S. Gao, C. Zhang, IEEE Trans. Electron Devices **67**, 4884–4890 (2020)
45. F.L. Faita, J.P.B. Silva, M. Pereira, M.J.M. Gomes, Appl. Phys. Lett. **107**, 242105 (2015)

Publisher's Note Springer Nature remains neutral with regard to jurisdictional claims in published maps and institutional affiliations.